DE GRUYTER Z. Naturforsch. 2020; 75(1–2)b: 41–50

Michael Küpers, Ralf Peter Stoffel, Barbara Bong, Markus G. Herrmann, Zikang Li, Alexander Meledin, Joachim Mayer, Karen Friese and Richard Dronskowski*

Preferred selenium incorporation and unexpected interlayer bonding in the layered structure of $Sb_2Te_{3-x}Se_x$

https://doi.org/10.1515/znb-2019-0101
Received June 25, 2019; accepted August 10, 2019

Abstract: We have performed a detailed structural analysis of several crystals from the $Sb_2Te_{3-x}Se_x$ solid solution (with $x=0$–1.55) using a combination of single-crystal and powder X-ray diffraction and high-resolution scanning transmission electron microscope imaging combined with energy-dispersive X-ray spectroscopic mapping. The experimental study was supported by quantum-chemical calculations. All compounds crystallize in the rhombohedral tetradymite structure type in which the atoms occupy three symmetrically independent crystallographic sites; the two chalcogenide sites A1 and A2, and the antimony site Sb. They form quintuple A2–Sb–A1–Sb–A2 layers perpendicular to the [001] direction, held together via A2–A2 chalcogenide-chalcogenide interactions. The results of our experimental study show unambiguously, and in agreement with quantum-chemical calculations, a preferred incorporation of selenium into the A2 position inside the layers. An unexpected increase of the van-der-Waals inter-layer distances is observed for low Se contents ($x<1$) and discussed with the help of DFT calculations.

Keywords: antimony telluride selenide; crystal-structure analysis; density-functional theory; transmission electron microscopy; van-der-Waals interaction.

Dedicated to: Professor Arndt Simon on the occasion of his 80th birthday.

1 Introduction

Antimony telluride, Sb_2Te_3, has been extensively studied due to its extraordinary physical properties like thermoelectricity [1, 2], as a topological insulator [3], or for its potential application in non-volatile phase-change memory devices [4]. It has been demonstrated that the phase-change properties of Sb_2Te_3 can be efficiently tuned by cationic substitution with elements such as Ge, In, or Ag [4]. Substitutions on the chalcogenide sites are less common but may also lead to interesting property changes. The pseudo-binary $Sb_2Te_{3-x}Se_x$ solid solution is a key system in this respect, and members of this system are also discussed as potential phase-change materials [5] or as topological insulators [6]. Unfortunately, a precise crystallographic characterization of the solid solution was missing up to now, a fact that strongly hampers the establishment of reliable structure-property relationships.

The crystal structure of Sb_2Te_3 (space group $R\bar{3}m$, No. 166) was first determined in the 1950s [37]. Within the structure three symmetry-independent sites are occupied: one antimony site (Wyckoff position $6c$ with $z=0.399$; site symmetry $3m$) and two chalcogenide sites (A1 on $3a$, site symmetry $\bar{3}m$, and A2 on $6c$ with $z=0.787$, site symmetry $3m$) occupied by Te. The atoms form quintuple A2–Sb–A1–Sb–A2 layers which are stacked along the c axis and held together via homoatomic, seemingly van-der-Waals-like A2–A2 interactions (Fig. 1a). The coordination polyhedra of each type of atom are shown in Fig. 1b. The Sb atoms are coordinated by three A1 and three A2 atoms resulting in a distorted octahedron. The A1 atoms are surrounded by six Sb atoms in a regular octahedral coordination whereas the A2 atoms are coordinated by three Sb atoms plus three longer bonds to three A2 atoms, beyond the van-der-Waals

---

***Corresponding author: Richard Dronskowski,** Institute of Inorganic Chemistry, RWTH Aachen University, 52056 Aachen, Germany; Jülich-Aachen Research Alliance (JARA-HPC), RWTH Aachen University, 52056 Aachen, Germany; and Hoffmann Institute of Advanced Materials, Shenzhen Polytechnic, 7098 Liuxian Blvd, Nanshan District, Shenzhen, P.R. China, e-mail: drons@HAL9000.ac.rwth-aachen.de
Michael Küpers, Ralf Peter Stoffel and Barbara Bong: Institute of Inorganic Chemistry, RWTH Aachen University, 52056 Aachen, Germany
Markus G. Herrmann, Zikang Li and Karen Friese: Jülich Center for Neutron Science-2/Peter Grünberg Institute-4, Forschungszentrum Jülich GmbH, 52425 Jülich, Germany
Alexander Meledin and Joachim Mayer: Central Facility for Electron Microscopy, RWTH Aachen University, 52056 Aachen, Germany; and Ernst Ruska-Centre for Microscopy and Spectroscopy with Electrons (ER-C), Forschungszentrum Jülich GmbH, 52425 Jülich, Germany

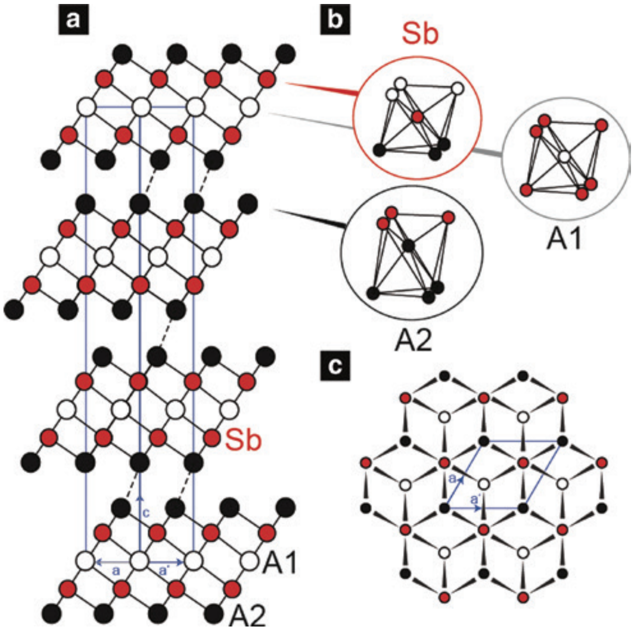

Fig. 1: Structure of Sb_2Te_3.
(a) Projections of the unit cell of Sb_2Te_3, built up from quintuple A2(Te)–Sb–A1(Te)–Sb–A2(Te) layers stacked along the *c* axis. (b) Coordination polyhedra of the three crystallographically independent sites. (c) Projection of the Sb_2Te_3 layer structure along [001].

interaction limit, resulting altogether in a strongly distorted octahedral motif.

The pseudo-binary phase diagram of $Sb_2Te_{3-x}Se_x$ was first studied in the 1960s [7, 8] and exhibits two single-phase regions. Crystals with x of up to 1.8 are isostructural to Sb_2Te_3 and form a solid solution in the tetradymite or Bi_2Te_3 structure type. Another single-phase region was found for high x values between 2.85 and 3 representing a solid solution in the orthorhombic Sb_2Se_3 structure type [9]. In-between these two single-phase regions ($1.8 < x < 2.85$) a miscibility gap has been identified, and a two-phase region in which the Sb_2Te_3 and Sb_2Se_3 structures co-exist was postulated.

By substituting tellurium by selenium, a preferred incorporation of selenium into the A1 position inside the quintuple layers was postulated by Ullner already in 1968 [10]. In 1974, Anderson et al. refined the crystal structure of Sb_2Te_2Se based on single-crystal data and claimed a Se/Te order in which Se exclusively occupies the A1 site while tellurium is located at A2 [11]. In that publication, however, one does not find any information as to whether the corresponding occupancies of the two anionic sites were refined or simply assumed by the authors.

In this work, we have performed a detailed structural analysis of several compounds in the stability field of the tetradymite structure type with representative compositions. The experimental investigations were supported by quantum-chemical calculations. Our study focuses on the changes in bonding behavior which are induced by the incorporation of selenium into the Sb_2Te_3 structure.

2 Experimental

2.1 Synthesis, single-crystal and powder diffraction

In a first step, powders of the end members Sb_2Te_3 and Sb_2Se_3 were synthesized from stoichiometrically weighed amounts of the elements (Sb: 99.9999%, Koch-Light Laboratories Limited; Se: 99.999%, MaTeck; Te: 99.999% ChemPur) in evacuated quartz ampoules at $T = 973$ K. Polycrystalline samples of $Sb_2Te_{3-x}Se_x$ ($x = 0$–1.8) were synthesized from stoichiometric amounts of the binary phases. For this, pellets of the starting materials were placed in glass ampoules which were sealed under Ar atmosphere. The ampoules were heated up to 773 K for 7 days and subsequently quenched to room temperature in air.

Low-temperature powder-diffraction measurements of the ground samples Sb_2Te_3, $Sb_2Te_{2.4}Se_{0.6}$, $Sb_2Te_{1.8}Se_{1.2}$, and $Sb_2Te_{1.2}Se_{1.8}$ were performed between 20 and 300 K, using a Huber G670 Guinier Camera equipped with a Ge(111) crystal monochromator, a closed-cycle He cryostat, and an image-plate detector. The samples were cooled down to $T = 20$ K with cooling rates of $5\ K \cdot min^{-1}$ and then equilibrated for 20 min. Powder patterns (Cu$K\alpha_1$ radiation; 0–100° in 2θ, $\Delta\theta = 0.005°$) were measured in steps of 5 K upon heating with a rate of $5\ K \cdot min^{-1}$ between each temperature point (dwell time of 5 min).

For the low-temperature powder-diffraction measurements, the lattice parameters were determined from Le Bail refinements [12] at each temperature using the program Jana2006 [13]. The background was described by 100 points and automatically fitted using a 20-parameter polynomial function. A pseudo-Voigt profile function with an angle-independent Lorentzian part and two Gaussian parameters (one angle-dependent and one angle-independent) were used, and the zero shift was refined. Lattice parameters given by Mansour et al. [14] for Sb_2Te_3 were used as starting values.

Single crystals of $Sb_2Te_{3-x}Se_x$ were grown by chemical vapor transport from the corresponding polycrystalline samples using iodine (99.5%, Merck) as transport agent at temperatures from 773 to 753 K over 18 h.

Table 1: Crystallographic data of the $Sb_2Te_{3-x}Se_x$ single-crystal refinements, space group $R\bar{3}m$ (no. 166).

Refined formula	Sb_2Te_3	$Sb_2Te_{2.64(1)}Se_{0.36(1)}$	$Sb_2Te_{2.38(1)}Se_{0.62(1)}$	$Sb_2Te_{2.11(2)}Se_{0.89(2)}$	$Sb_2Te_{2.01(1)}Se_{0.99(1)}$	$Sb_2Te_{1.81(1)}Se_{1.19(1)}$	$Sb_2Te_{1.67(1)}Se_{1.33(1)}$	$Sb_2Te_{1.45(1)}Se_{1.55(1)}$
Formula mass	626.3	608.63	596.14	583.01	578.15	568.42	561.61	550.91
Lattice parameter								
a, Å	4.2714(6)	4.2459(3)	4.2132(6)	4.201(3)	4.1919(5)	4.1757(3)	4.1646(3)	4.1556(11)
c, Å	30.459(4)	30.339(5)	30.100(9)	30.01(2)	29.939(4)	29.861(4)	29.793(4)	29.772(8)
Volume V, Å^3	481.3(2)	473.66(10)	462.72(19)	458.7(5)	455.61(10)	450.91(8)	447.50(8)	445.3(2)
Density d, g cm^{-3}	6.483	6.401	6.418	6.382	6.321	6.280	6.252	6.164
Abs. coeff. μ, mm^{-1}	21.643	22.439	23.294	23.726	24.133	24.644	25.015	24.707
T_{min}; T_{max}	0.4847; 0.7461	0.4303; 0.7461	0.5280; 0.7459	0.4305; 0.7461	0.3808; 0.7461	0.3808; 0.7461	0.2296; 0.7461	0.3872; 0.7460
θ range	2.01–30.80	2.014–30.980	2.030–29.847	2.04–30.80	2.04–30.90	2.05–30.79	2.05–31.09	2.05–30.53
hkl range	−5, 6; −6, 3; −39, 42	−6, 5; −4, 5; −33, 42	−3, 5; −5, 5; −42, 40	−6, 5; −5, 5; −41, 30	−6, 4; −3, 5; −41, 41	−5, 2; −5, 6; −40, 41	−5, 5; −5, 5; −40, 34	−5, 5; −5, 5; −41, 29
No. of refl.	1304	1266	1234	956	1222	941	1183	1147
No of indep. refl.	227	227	212	216	215	209	213	209
No of parameters	10	11	11	11	12	11	12	12
R_1; wR_2 (all data)	0.0202; 0.0426	0.0243; 0.0513	0.0433; 0.0692	0.0402; 0.0762	0.0165; 0.0358	0.0259; 0.0581	0.0271; 0.0645	0.0299; 0.0675
GOF	1.126	1.096	1.096	1.068	1.142	1.141	1.221	1.25
Atomic positions								
Sb (6*a*)	0.39864(2)	0.39724(2)	0.39550(3)	0.39475(3)	0.39417(2)	0.39426(2)	0.39448(2)	0.39516(2)
A2 (6*c*)	0.21221(2)	0.21313(2)	0.21415(3)	0.21459(3)	0.21485(2)	0.21482(2)	0.21467(2)	0.21431(2)
Occupancies of Te								
A2	1	0.979(7)	0.997(13)	0.95(2)	0.954(6)	0.882(9)	0.823(7)	0.701(7)
A1	1	0.691(8)	0.39(2)	0.21(2)	0.104(7)	0.042(10)	0.024(9)	0.046(9)
Anisotropic displacement parameters								
Sb								
U_{11}	0.0175(29	0.0182(3)	0.0174(4)	0.0158(4)	0.01585(19)	0.0156(3)	0.0175(3)	0.0174(3)
U_{33}	0.0232(3)	0.0287(3)	0.0269(6)	0.0299(6)	0.0229(3)	0.0206(4)	0.0206(4)	0.0235(4)
U_{12}	0.00873(11)	0.00908(13)	0.0087(2)	0.00789(18)	0.00793(10)	0.00779(13)	0.00875(15)	0.00868(14)
A2								
U_{11}	0.0153(2)	0.0167(2)	0.0168(4)	0.0149(3)	0.01496(18)	0.0144(2)	0.0164(3)	0.0158(3)
U_{33}	0.0135(3)	0.0190(3)	0.0191(6)	0.0236(5)	0.0165(2)	0.0168(3)	0.0184(3)	0.240(4)
U_{12}	0.00763(10)	0.00837(10)	0.00838(18)	0.00747(16)	0.00748(9)	0.00722(11)	0.0822(13)	0.00791(13)
A1								
U_{11}	0.0133(2)	0.0127(3)	0.0146(6)	0.0135(6)	0.0129(3)	0.0127(4)	0.0150(4)	0.0149(4)
U_{33}	0.0124(3)	0.0154(4)	0.0148(9)	0.0201(8)	0.0149(4)	0.0137(6)	0.0133(6)	0.0171(6)
U_{12}	0.00663(11)	0.00637(14)	0.0073(3)	0.0067(3)	0.00643(15)	0.0063(2)	0.0075(2)	0.0074(2)

Single-crystal diffraction data were measured on a Bruker SMART APEX diffractometer with Mo$K\alpha$ radiation. The integration was performed with SAINT+, and a multi-scan absorption correction using the program SADABS [15, 16] was applied. The structure was solved using direct methods (SHELXS [17]). Subsequent least-squares refinements based on F^2 were performed with the program SHELXL [18]. Selected crystallographic data are given in Table 1.

Further details concerning data collection and refinement can be obtained from the Fachinformationszentrum Karlsruhe, 76344 Eggenstein-Leopoldshafen, Germany (fax: +49-7247-808-666; e-mail: crysdata@fiz-karlsruhe.de) on quoting the deposition numbers CSD-1898610–1898617.

2.2 TEM

To independently validate the XRD results in real space, phases with the compositions $Sb_2Te_{2.4}Se_{0.6}$, $Sb_2Te_{1.8}Se_{1.2}$ and $Sb_2Te_{1.2}Se_{1.8}$ were studied by TEM. For TEM measurements lamellae were prepared using a focused ion beam (FIB) technique employing a FEI Dual Beam Helios NanoLab system. The lamellas were cut along the *c* axis of $Sb_2Te_{3-x}Se_x$ single crystals.

The High Resolution High Angle Annular Dark Field Scanning Transmission Electron Microscopy (HR HAADF STEM) combined with STEM energy-dispersive X-ray spectroscopy (STEM-EDX) mappings was carried out on an FEI Titan ChemiSTEM probe Cs-corrected TEM operated at 200 kV [19]. For EDX mapping a Bruker "Super-X" wide solid angle EDX detector was used at a voltage of 200 kV [20].

2.3 Quantum-chemical calculations

Density-functional theoretical calculations were carried out using the Vienna ab initio simulation package (VASP) [21]. The projector-augmented wave method [22] was used together with the local-density approximation [23] to account for exchange and correlation. Plane-wave basis sets with kinetic energies up to 500 eV were used.

The structures for the solid-solution phases were set up based on a 2×2×1 supercell of Sb_2Te_3 in the hexagonal setting containing 12 formula units and 60 atoms. For each composition, six setups were created, three models with a random substitution and three with partially ordered substitution of Se for Te. For the "disordered" model, the Te atoms were replaced randomly by Se with increasing Se content *x*. For the partially "ordered" structures, first the tellurium atoms on the Te1 site were replaced by Se and, once the site was fully occupied by Se ($x=1$), the tellurium atoms on the Te2 sites were randomly substituted by selenium.

3 Results and discussion

Figure 2a shows the Se site-occupancy factors of the A1 and A2 sites obtained from our single-crystal structure refinements as a function of the selenium content *x*. Clearly, for $x \leq 1$ the selenium atoms are preferably incorporated into the A1 position, however, a refinement of the site occupancy factor of the A2 site indicates that there is also a small selenium content (below 5%) on this site for all investigated crystals, which was not reported before. For higher Se contents ($x > 1$), the Te on the A2 position is substituted by Se. It is noteworthy that even for the highest selenium contents, a small percentage of tellurium is still present on

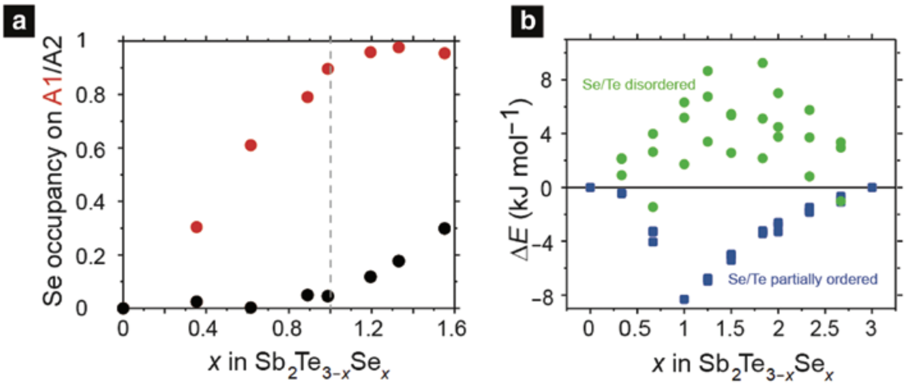

Fig. 2: Selenium occupancies and formation energies.
(a) Selenium occupancies of the chalcogenide positions A1 (red) and A2 (black) as a function of the Se content. (b) Theoretical formation energies of the different solid-solution compounds related to Sb_2Se_3 and (hexagonal) Sb_2Te_3. Green: selenium and tellurium atoms are randomly distributed on the chalcogenide sites; blue: selenium is first incorporated on the A1 site.

the A1 position. Our single-crystal data of the $Sb_2Te_{3-x}Se_x$ samples with $x = 0–1.55$ therefore clearly shows a preferred incorporation of selenium into the A1 position and, thus, they are in full accordance with the literature [11].

Independent theoretical electronic-structure considerations confirm the preferred incorporation of selenium at the A1 position. In Fig. 2b we present the relative formation energies ΔE of $Sb_2Te_{3-x}Se_x$ solid-solution crystals with numerical entries for randomly distributed and partially ordered Se/Te occupation. These energies are related to those of the end member phases, Sb_2Te_3 and Sb_2Se_3, where the latter was also referred to the rhombohedral Bi_2Te_3 structure type, via $\Delta E = E(Sb_2Te_{3-x}Se_x) - (3 - x)/3\ E(Sb_2Te_3) - x/3\ E(Sb_2Se_3)$. The data clearly reflect that there is a gain in energy by the preferred incorporation of selenium into the center of the quintuple layers, the minimum of $\Delta E = 8.3$ kJ mol^{-1} occurring at $x = 1$. For this composition, the (theoretical) structure is completely ordered with selenium at the A1 site and tellurium on the A2 site. Obviously, a random Se incorporation leads to energies which are both higher than the energies of (a) the pure end members and of (b) the solid-solution phases assuming an ordered distribution of the two chalcogenide anions.

Figure 3 shows HR HAADF STEM Z-contrast images of pristine Sb_2Te_3 and $Sb_2Te_{1.2}Se_{1.8}$ taken along the [100] axis together with the corresponding integrated line profiles along the c axis. The image reflects the tetradymite structure of the $Sb_2Te_{1.2}Se_{1.8}$ sample. The intensities seen in these HAADF STEM images are roughly proportional to the atomic number $Z^{1.7}$ [24]; hence they enable a direct interpretation. The lighter Sb has a slightly smaller atomic number than Te ($Z_{Sb} = 51$ and $Z_{Te} = 52$) and, therefore, it appears as darker spots when compared to tellurium. Nonetheless, the A1 and A2 positions even in a pristine Sb_2Te_3 specimen appear with a different contrast due to the different coordination. A1 placed in the middle of the quintuple block shows a higher contrast than the A2 position which is situated next to the van-der-Waals gap.

In contrast to the end member Sb_2Te_3, the $Sb_2Te_{1.2}Se_{1.8}$ sample shows the opposite tendency because the Sb sites appear brighter than the Te sites. This already confirms that the lighter Se ($Z_{Se} = 34$) is incorporated into the Te positions. Besides that, the line scan shows a lower intensity for the A1 position when compared to A2, indicating the preferred incorporation of selenium at A1.

Figure 4a shows the HAADF STEM Z-contrast image of the mapped region together with EDX of elemental Sb, Te, Se and composite HAADF STEM/Sb/Te/Se maps of the $Sb_2Te_{1.8}Se_{1.2}$ sample. The Se-filtered map and the composite figure clearly visualize that the A1 position inside the layer is mainly occupied by selenium, while the outer A2 position is characterized by a mixed occupancy of selenium and tellurium. In other words, these results are fully matching those from the single-crystal XRD measurements. The almost perfect match between the XRD data and the EDX mapping continues for the $Sb_2Te_{2.4}Se_{0.6}$ and $Sb_2Te_{1.2}Se_{1.8}$ compositions, as seen from Fig. 4b.

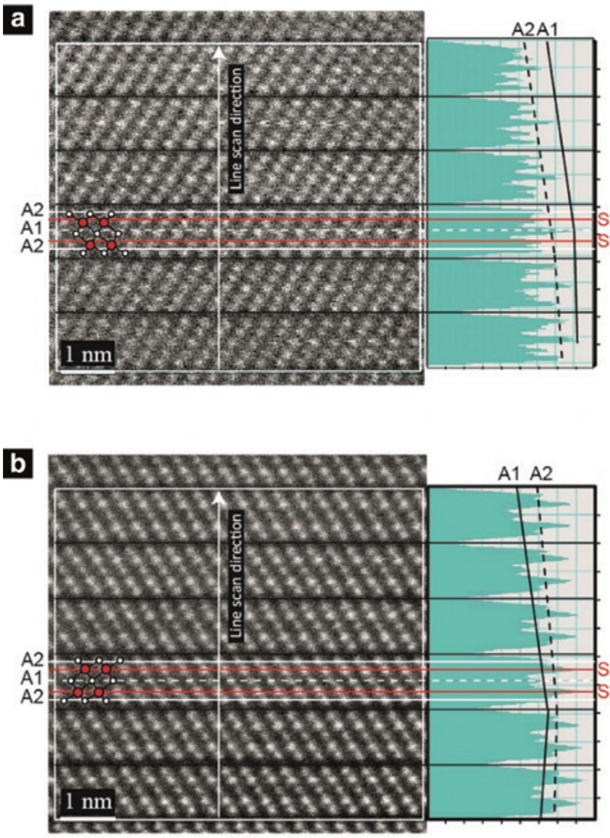

Fig. 3: HAADF-STEM images of Sb_2Te_3 and $Sb_2Te_{1.2}Se_{1.8}$. HAADF-STEM images of (a) pristine Sb_2Te_3 and (b) $Sb_2Te_{1.2}Se_{1.8}$ taken along the [100] zone axis together with corresponding line scans along the c axis.

The interatomic distances and bond angles of several $Sb_2Te_{3-x}Se_x$ crystals are presented in Fig. 5a–c. Because of the high symmetry of the tetradymite structure, only two symmetry-independent Sb–A distances (d_{Sb-A1}; d_{Sb-A2}) and three interatomic angles (A1–Sb–A1; A2–Sb–A2 and A1–Sb–A2) around the Sb position are to be considered (Fig. 5a). Figure 5b shows the heteroatomic distances d_{Sb-A1} and d_{Sb-A2} as a function of the compositional parameter x. For pure Sb_2Te_3 the distance $d_{Sb-A2} = 2.9954(5)$ Å is close to the ideal distance between ions of the two elements expected for an octahedrally coordinated Sb–Te system (2.97 Å) [25], while d_{Sb-A1} is significantly longer (3.17 Å), indicating a different bonding nature. For small selenium contents, the distance between Sb and A1 decreases upon increasing Se content, while d_{Sb-A2} seems to be nearly constant up to $x = 1$.

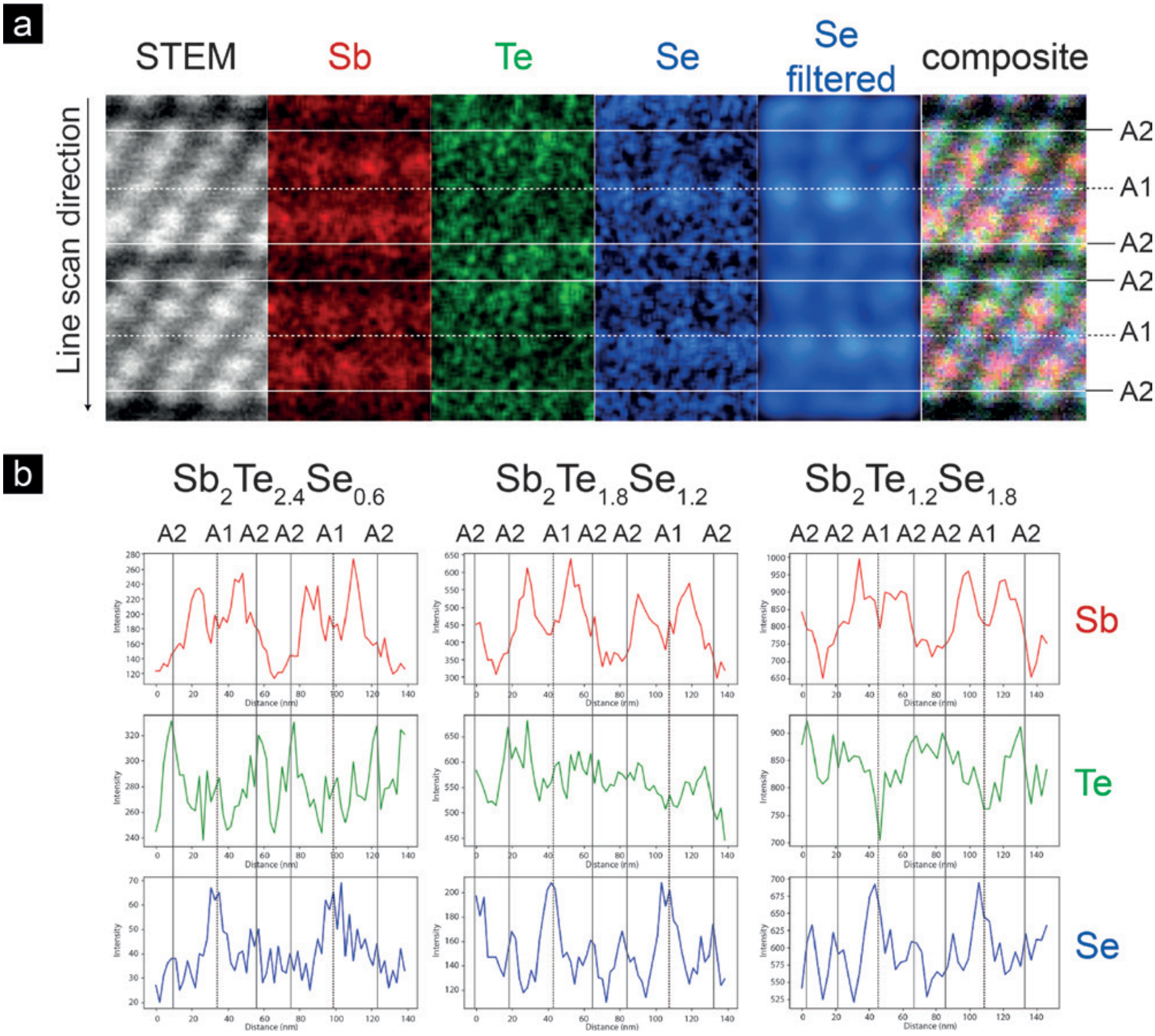

Fig. 4: ADF STEM image and elemental EDX maps from the $Sb_2Te_{3-x}Se_x$ solid solution.
(a) ADF STEM image together with elemental EDX Sb, Te, Se (red, green blue) maps of $Sb_2Te_{1.8}Se_{1.2}$. (b) Line scans of elemental EDX profiles across similar regions for all three studied compositions $Sb_2Te_{2.4}Se_{0.6}$, $Sb_2Te_{1.8}Se_{1.2}$, and $Sb_2Te_{1.2}Se_{1.8}$.

Obviously, the preferred selenium incorporation inside the layers affects only the Sb–A1 bond whereas $d_{Sb–A2}$ remains essentially unchanged. Above $x = 1$ the A1 position is almost completely occupied with selenium and the Sb–A1 distance remains constant and, thus, the bond length is not affected by the Se incorporation into the A2 site. On the other hand, $d_{Sb–A2}$ at the periphery of the layers starts to slightly *decrease* with an *increasing* Se content on this position.

For the solid-solution phases, the values for $d_{Sb–A1}$ and $d_{Sb–A2}$ can also be derived from DFT. The calculations arrive at two values for each Sb–A distance, one for the Sb–Se and one for the Sb–Te combination. As depicted in Fig. 5b, for the end member Sb_2Te_3, the $d_{Sb–Te2}$ distance is in perfect agreement with the experimental data, while the distance $d_{Sb–Te1}$ is slightly underestimated. The theoretically predicted value for the $d_{Sb–Te2}$ distance is in good agreement with experimental data up to a Se content of $x < 1$ (where hardly any Se is incorporated into the A2 site). For higher Se contents ($x > 1$), when Se starts to occupy the A2 site, the theoretical $d_{Sb–Te}$ distance is slightly overestimated, while at the same time the theoretical $d_{Sb–Se2}$ distance is clearly too small. As the diffraction experiment only sees an Se/Te *average* position with Te being the stronger scatterer, the smaller Sb–Se2 distance as given by theory is less visible within XRD. In the same spirit, the theoretically predicted Sb–Se1 distance for low Se contents ($x < 1$)

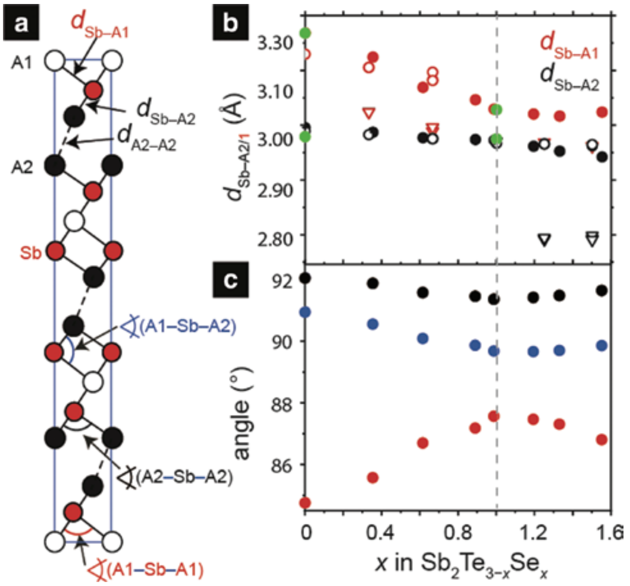

Fig. 5: Interatomic distances and angles in the $Sb_2Te_{3-x}Se_x$ solid solution.
(a) Projection of the $Sb_2Te_{3-x}Se_x$ structure (b) Experimentally determined distances between the Sb site and the A1 (red) and A2 (black) sites are shown (filled circles) and compared to theoretical values (open circles: Sb–Te; open triangles Sb–Se bonds). Literature values from Anderson et al. are shown in green [11]. (c) Interatomic angles of the SbA_6 octahedron are also shown.

is smaller than the average value, while the theoretical Sb–Te1 distance is closer to the experiment. Nonetheless, the general trend of the Sb–A1 distance as a function of Se content is well reproduced throughout.

In Fig. 5c, the experimentally determined angles A1–Sb–A1, A1–Sb–A2 and A2–Sb–A2 are shown as a function of the selenium content. For pure Sb_2Te_3 we observe a maximum deviation between the three angles indicating the largest degree of octahedral distortion. By replacing tellurium in the A1 position with selenium, the distortion of the octahedra decreases, and the angles are getting closer to the ideal octahedral angle of 90°. For the almost completely ordered compound Sb_2Te_2Se, we find the minimum angular spread and the smallest deviations from 90°. For Se contents $x > 1$, the distortion of the octahedra starts to increase again.

Figure 6a shows the experimental and theoretically predicted interlayer distances d_{A2-A2} as a function of the selenium content. The experimental data exhibit an unexpected behavior while the selenium amount increases. In contrast to the heteroatomic distances, d_{A2-A2} *increases* with increasing selenium content up to a maximum value of $x = 1$. This is rather unexpected since – as we have shown before – for these selenium contents, there is next to no Se present on the A2 site and thus, one would expect that the interlayer distances remain unchanged. This strange behavior indicates, however, that an incorporation of selenium into the central position of the layer *weakens* the interaction between the layers. The theoretical data fully corroborate the experimental observation, and also the interatomic distances reported in the literature for Sb_2Te_3 and Sb_2Te_2Se are in good agreement [11] (see Fig. 6a).

Recently, low-temperature heat-capacity data of several $Sb_2Te_{3-x}Se_x$ solid-solution crystals have been reported [29] and it was concluded that the incorporation of selenium into the Sb_2Te_3 structure type leads to an increasing bond polarity as a consequence of the replacement of Te by the more electronegative selenium. The unexpected elongation of the interlayer distance d_{A2-A2} can be explained, at least qualitatively, as a secondary effect: the increasing polarity inside the layer attracts more electron density from the periphery of the layer and leads to a weakening of the interlayer interactions. At x values larger than 1, the interlayer distance shrinks again because the smaller Se enters the A2 position and, thus, weakens the repulsion between neighboring layers.

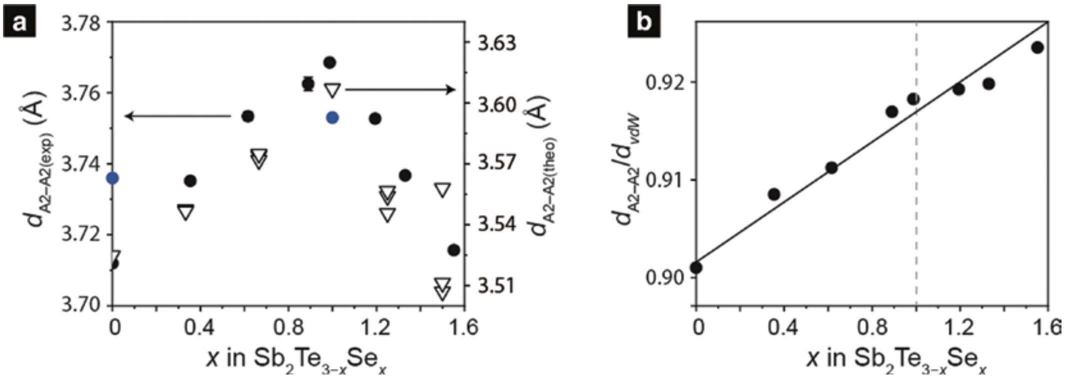

Fig. 6: Experimental and theoretical van-der-Waals distances.
(a) d_{A2-A2} distances from experiment (black circles), theory (black open triangles) and literature (blue circles) [11]. (b) Ratios between experimental d_{A2-A2} and literature values for van-der-Waals distances d_{vdW}.

As pointed out already, the relative change of d_{A2-A2} is perfectly reproduced in the values obtained from electronic-structure theory, despite the fact that the absolute values are slightly underestimated. This underestimation is due to the fact that the van-der-Waals gaps are hard to model by quantum-chemical calculations based on density-functional theory. We have recently proven the reliability of the LDA functional for the case of Sb_2Te_3 where the lattice parameters as given by LDA calculations are qualitatively comparable to those using explicit van-der-Waals corrections [26], so a different (and far more expensive) theoretical approach is unlikely to further improve the agreement between experiment and theory.

Intuitively, one might consider the interlayer distance d_{A2-A2} in Sb_2Te_3 as a typical van-der-Waals contact – as was indeed assumed in the literature – but this looks like an oversimplification in the present case. The van-der-Waals radius of tellurium according to Bondi is 2.06 Å [27] and, therefore, one would expect a Te–Te van-der-Waals distance around 4.12 Å. However, from our structural analysis we have determined a value of 3.7120(7) Å for the A2–A2 bond length which is about 10% smaller than the expected value. In other words, there must be some *additional attractive* contribution to the weak Te–Te interactions which leads to a pronounced shortening of these bonds.

The ideal van-der-Waals bond length d_{vdw} for the $Sb_2Te_{3-x}Se_x$ solid-solution crystals can be calculated from the site occupancy factor x_{Ch} and the Bondi radii of the chalcogenide r_{Ch} as an arithmetic average:

$$d_{vdW} = 2\Sigma x_{Ch} r_{Ch}$$

The ratio between the experimentally determined A2–A2 distance and the ideal van-der-Waals bond length (d_{vdW}), calculated from the experimentally refined occupancies of the A2 position, is shown in Fig. 6b. For all compounds, the ratio is clearly below 1, so that all experimental A2–A2 distances are “too short” with respect to the corresponding ideal value. The ratio shows an almost linear increase, with a little shoulder at $x=1$, indicating that incorporating selenium results in a weakening of the interlayer interactions which, once again, must be stronger than what would be expected from a typical van-der-Waals contact. Also, this behavior depends on the selenium content, rather than on the preferred selenium incorporation on the A1 position. As mentioned before, the elongation of the A2–A2 distance can be explained by the increasing polarity of the antimony-chalcogenide bonds inside the layers, but it does *not* explain why these bonds are much shorter than expected for a van-der-Waals contact in the first place.

Table 2: Experimentally found chalcogenide–chalcogenide distances in various phases and their relationship with tabulated van-der-Waals distances.

Compound	d_{A-A} (Å)	d_{A-A}/d_{vdW}	Reference
Sb_2Te_3	3.7120(7)	0.88	This work
Bi_2Te_3	3.636(5)	0.87	[29]
Bi_2Se_3	3.480(9)	0.92	[30]
$Ge_2Sb_2Te_5$	3.740(2)	0.91	[31]
Ge_4Se_3Te	3.802(3)	0.98	[32]
GaGeTe	4.131(6)	1.00	[33]
GaSe	3.81(3)–3.94(3)	1.00–1.03	[34]
$SnSe_2$	3.776(2)	0.99	[35]
$Si_{1.67}Te_3$	4.008(2)	0.97	[36]

In order to understand the origin of the comparably short A2–A2 interactions in detail, we have compared the interlayer distances of several compounds with the tetradymite structure type (and related structures such as $Ge_2Sb_2Te_5$) to the corresponding value determined for Sb_2Te_3 (Table 2). The too short interlayer van-der-Waals bond lengths for *some of* those materials suggest the presence of additional attractive interactions between the layers that go beyond classical van-der-Waals forces. It should be pointed out in this context that the unusual behavior of some of these compounds and the relation to the underlying bonding scheme are currently under discussion [28] and are discussed to be partly responsible for the interesting physical properties (e.g. thermoelectricity, phase-change applications, topological insulators) which are not observed for materials with classical van-der-Waals bonds.

The experimentally determined c/a lattice-parameter ratio obtained from powder-diffraction measurements are shown in Fig. 7 and compared to the corresponding data from theoretical calculations. Due to the strongly anisotropic nature of the crystal structure, large c/a ratios of about 7 were found. With increasing selenium content, the c/a ratios increase. Around $x=1$ one observes a slight shoulder in the increase which is also reflected in the theoretical data. The absolute computational values are smaller than the experimental ones, which is due to the fact that the van-der-Waals interactions along c are hard to describe by quantum-chemical calculations.

The increasing c/a parameter as a function of the compositional parameter x indicates that the decrease of a is stronger than the decrease of the c, as also reflected from the individual bond lengths derived from the single-crystal diffraction measurements. The homoatomic A2–A2 van-der-Waals-like bonds mainly contribute to the c lattice parameter, while the heteroatomic bonds are mostly oriented in the ab plane, contributing mainly to

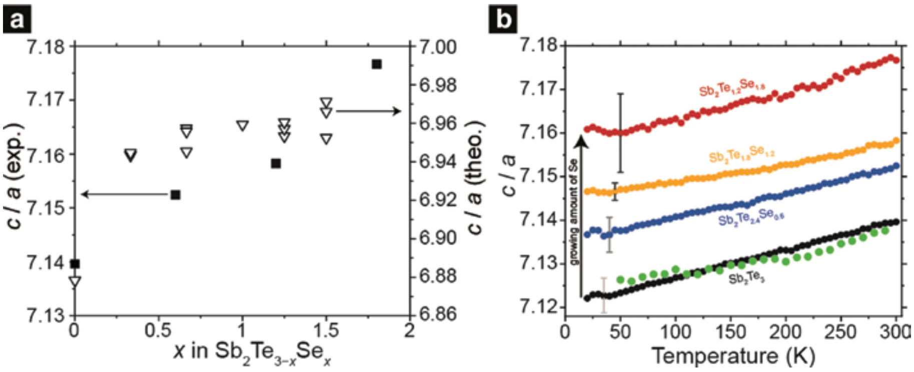

Fig. 7: Experimental and theoretical *c*/*a* ratios.
(a) *c*/*a* ratios determined from experiment at $T=300$ K (black squares) and theory (triangles). (b) Temperature-dependence of the *c*/*a* ratio of several $Sb_2Te_{3-x}Se_x$ compounds (black, blue yellow, red). For comparison data for Sb_2Te_3 from literature (green) [1] are included. Error bars are shown for one refinement per composition.

the *a* parameter. Therefore, the observed increase of d_{A2-A2} for $x<1$, together with the decrease of the heteroatomic bonds, lead to the observed increase of *c*/*a*. The absolute changes of the heteroatomic bond length d_{Sb-A1} and d_{Sb-A2} are much larger than those for d_{A2-A2} leading to an increase of *c*/*a* even for $x>1$, where both bond length decrease.

Figure 7b shows the temperature-dependent *c*/*a* ratios for selected compounds from the $Sb_2Te_{3-x}Se_x$ system. For Sb_2Te_3, the values are compared to literature values [1]. With decreasing temperature, the *c*/*a* ratio shows an almost linear decrease down to around 50 K for all samples. In general, the thermal behaviour demonstrates that the decrease in the *c* lattice parameter as a function of decreasing temperature is more pronounced than the decrease in the *a* lattice parameter. This suggests that the van-der-Waals-like interactions between the layers are more influenced by the temperature than the strong heteroatomic covalent bonds within the layer. The change in trend for *c*/*a* around $T=50$ K could indicate that the van-der-Waals-like interactions reach their energetic minimum (strongest interaction) at this temperature.

4 Conclusion

For the first time, a detailed structural characterization of the solid solution $Sb_2Te_{3-x}Se_x$ with $x=0$–1.5 adopting the Bi_2Te_3 structure type was performed using a combination of single-crystal and temperature-dependent X-ray diffraction measurements, HR-TEM imaging, EDS mapping, and quantum-chemical calculations. Both experimental and theoretical results indicate a preferred incorporation of selenium into the central A1 site of the quintuple layers. The A2–A2 interlayer distance in Sb_2Te_3 is significantly smaller than expected for a conventional Te–Te van-der-Waals interaction. This behavior can also be observed for similar tetradymite-type compounds despite the fact that other layered structure types exhibit expected van-der-Waals distances. An unexpected increase of the interlayer distances in $Sb_2Te_{3-x}Se_x$ was observed upon Se incorporation and leads to a maximum distance for $x=1$. We explain this phenomenon by the increasing binding polarity of the Sb–A1 and Sb–A2 bonds which pulls electron density into the layers and, therefore, weakens the interlayer bonding.

Acknowledgements: This work was supported by the Deutsche Forschungsgemeinschaft within the SFB Nanoswitches (SFB 917). We thank the Jülich-Aachen Research Alliance (JARA) as well as the RWTH Aachen University IT Center for providing CPU time within the JARA-HPC project “jara0033”.

References

[1] D. Bessas, I. Sergueev, H. C. Wille, J. Perßon, D. Ebling, R. P. Hermann, *Phys. Rev. B* **2012**, *86*, 224301.
[2] R. J. Mehta, Y. Zhang, C. Karthik, B. Singh, R. W. Siegel, T. Borca-Tasciuc, G. Ramanath, *Nat. Mater.* **2012**, *11*, 233.
[3] J. Tominaga, A. V. Kolobov, P. J. Fons, X. Wang, Y. Saito, T. Nakano, M. Hase, S. Murakami, J. Herfort, Y. Takagaki, *Sci. Technol. Adv. Mater.* **2015**, *16*, 014402.
[4] M. Wuttig, N. Yamada, *Nat. Mater.* **2007**, *6*, 824–832.
[5] D. P. Gosain, T. Shimizu, M. Ohmura, M. Suzuki, T. Bando, S. Okano, *J. Mater. Sci.* **1991**, *26*, 3271–3274.
[6] I. Efthimiopoulos, J. Zhang, M. Kucway, C. Park, R. C. Ewing, Y. Wang, *Sci. Rep.* **2013**, *3*, 2665.
[7] K. K. Palkina, V. G. Kuznetsov, *Izv. Akad. Nauk SSSR, Neorg. Mater.* **1965**, *1*, 2158–2164.
[8] I. Teramoto, S. Takayanagi, *J. Phys. Chem. Solids* **1961**, *19*, 124–129.

[9] H. Liu, C. R. Knowles, L. L. Y. Chang, *Can. Mineral.* **1995**, *33*, 115–128.

[10] H. A. Ullner, *Ann. Phys.* **1968**, *476*, 45–56.

[11] T. L. Anderson, H. B. Krause, *Acta Crystallogr.* **1974**, *B30*, 1307–1310.

[12] A. Le Bail, H. Duroy, J. L. Fourquet, *Mater. Res. Bull.* **1988**, *23*, 447–452.

[13] V. Petříček, M. Dušek, L. Palatinus, *Z. Kristallogr.* **2014**, *229*, 345.

[14] A. N. Mansour, W. Wong-Ng, Q. Huang, W. Tang, A. Thompson, J. Sharp, *J. Appl. Phys.* **2014**, *116*, 083513.

[15] SADABS (version 2004/1), Bruker AXS Inc., Madison, WI (USA) **2004**.

[16] SAINT+ (version 7.68), Bruker AXS Inc., Madison, WI (USA) **2009**.

[17] G. Sheldrick, *Acta Crystallogr.* **2008**, *A64*, 112–122.

[18] G. Sheldrick, *Acta Crystallogr.* **2015**, *C71*, 3–8.

[19] M. Heggen, M. Luysberg, K. Tillmann, *J. Large-Scale Res. Facil. JLSRF* **2016**, *2*, A42.

[20] A. Kovács, R. Schierholz, K. Tillmann, *J. Large-Scale Res. Facil. JLSRF* **2016**, *2*, A43.

[21] G. Kresse, J. Furthmüller, *Comput. Mater. Sci.* **1996**, *6*, 15–50.

[22] P. E. Blöchl, *Phys. Rev. B* **1994**, *50*, 17953–17979.

[23] J. P. Perdew, A. Zunger, *Phys. Rev. B* **1981**, *23*, 5048–5079.

[24] R. Erni, *Aberration-Corrected Imaging in Transmission Electron Microscopy: An Introduction*, Imperial College Press, London, **2010**.

[25] A. F. Holleman, N. Wiberg, E. Wiberg, *Lehrbuch der Anorganischen Chemie*, 102. Auflage, De Gruyter, Berlin, Boston, **2007**.

[26] R. P. Stoffel, V. L. Deringer, R. E. Simon, R. P. Hermann, R. Dronskowski, *J. Phys.: Condens. Matter* **2015**, *27*, 085402.

[27] A. Bondi, *J. Phys. Chem.* **1964**, *68*, 441–451.

[28] M. Wuttig, V. L. Deringer, X. Gonze, C. Bichara, J.-Y. Raty, *Adv. Mater.* **2018**, *30*, 1803777.

[29] V. V. Atuchin, T. A. Gavrilova, K. A. Kokh, N. V. Kuratieva, N. V. Pervukhina, N. V. Surovtsev, *Solid State Commun.* **2012**, *152*, 1119–1122.

[30] C. Pérez Vicente, J. L. Tirado, K. Adouby, J. C. Jumas, A. A. Touré, G. Kra, *Inorg. Chem.* **1999**, *38*, 2131–2135.

[31] P. Urban, M. N. Schneider, L. Erra, S. Welzmiller, F. Fahrnbauer, O. Oeckler, *CrystEngComm* **2013**, *15*, 4823–4829.

[32] M. Küpers, P. M. Konze, S. Maintz, S. Steinberg, A. M. Mio, O. Cojocaru-Mirédin, M. Zhu, M. Müller, M. Luysberg, J. Mayer, M. Wuttig, R. Dronskowski, *Angew. Chem. Int. Ed.* **2017**, *56*, 10204–10208.

[33] D. Fenske, H. G. von Schnering, *Angew. Chem. Int. Ed. Engl.* **1983**, *22*, 407–408.

[34] A. Kuhn, R. Chevalier, A. Rimsky, *Acta Crystallogr.* **1975**, *B31*, 2841–2842.

[35] G. Busch, C. Fröhlich, F. Hulliger, E. Steigmeier, *Helv. Phys. Acta* **1961**, *34*, 359–368.

[36] K. C. Göbgen, S. Steinberg, R. Dronskowski, *Inorg. Chem.* **2017**, *56*, 11398–11405.

[37] E. Dönges, *Z. Anorg. Allg. Chem.* **1951**, *265*, 56–61.